Effects of ion composition on escape and morphology at Mars

Qi Zhang[1,2], Mats Holmström[1], and Xiao-Dong Wang[1]

[1]Swedish Institute of Space Physics, Kiruna, Sweden
[2]Department of Physics, Umeå University, Umeå, Sweden

Correspondence: Qi Zhang (qizhang@irf.se)

Abstract. We refine a recently presented method to estimate ion escape from non-magnetized planets and apply it to Mars. The method combines in-situ observations and a hybrid plasma model (ions as particles, electrons as a fluid). We use measurements from the Mars Atmosphere and Volatile Evolution (MAVEN) mission and Mars Express (MEX) for one orbit on 2015-03-01. Observed upstream solar wind conditions are used as input to the model. We then vary the total ionospheric ion upflux until the solution fits the observed bow shock location. This solution is a self-consistent approximation of the global Mars-solar wind interaction at this moment, for the given upstream conditions. We can then study global properties, such as the heavy ion escape rate. Here we investigate the effects on escape estimates of assumed ionospheric ion composition, solar wind alpha particle concentration and temperature, solar wind velocity aberration, and solar wind electron temperature. We also study the amount of escape in the ion plume and in the tail of the planet. Here we find that estimates of total heavy ion escape are not very sensitive to the composition of the heavy ions, or the amount and temperature of the solar wind alpha particles. We also find that velocity aberration has a minor influence on escape, but that it is sensitive to the solar wind electron temperature. The plume escape is found to contribute 29% of the total heavy ion escape, in agreement with observations. Heavier ions have a larger fraction of escape in the plume compared to the tail. We also find that the escape estimates scales inversely with the square root of the atomic mass of the escaping ion specie.

1 Introduction

Atmospheric escape is an important process in the Martian climate evolution (Jakosky, 2017). For present Mars, the dominant escape of atmospheric neutrals is through four channels: Jeans escape (Chaffin, 2017; Jakosky, 2018), photochemical reactions (Fox and Hać, 2009; Lillis, 2017), sputtering (Leblanc, 2018) and electron impact ionization (Zhang, 2020). Ions above the exobase get accelerated by the solar wind electric field and can escape. Measurements from Phobos 2 (Lundin, 1989), MEX (Barabash, 2007; Nilsson, 2021) and MAVEN (Dong, 2017) and estimates from magnetohydrodynamic (MHD) (Ma and nagy, 2007; Regoli, 2018) and hybrid (Ledvina, 2017) models indicate that the heavy ions escape rate on Mars is between $10^{23} - 10^{25} s^{-1}$. The parameters affecting the solar wind interaction with the Martian atmosphere have been investigated, including the upstream conditions like extreme ultraviolet (EUV) radiation and solar wind dynamic pressure (Dong, 2017; Nilsson, 2021; Ramstad, 2021), and crustal magnetic fields (Fang, 2015; Ramstad, 2016; Weber, 2021).

Not only the number of the escaping ions is of interest, but also the composition and morphology contribute to the understanding of ion escape. Observations has identified O^+, O_2^+ and CO_2^+ as the major escaping species (Carlsson, 2006; Rojas, 2018;

Inui, 2019). These are also the species commonly used when modeling the interaction between Mars and the solar wind, using MHD or hybrid models (Harnett, 2006; Ma, 2019). The morphology of the escaping ions has been observed to follow two broad pathways (Dong, 2015, 2017; Dubinin, 2017; Nilsson, 2021). The solar wind convective electric field accelerates ions

30 into what is usually denoted as the ion plume at Mars. There is also a more fluid-like escape of ions into the tail region behind the planet. These two pathways has also been seen both in observations (Dong, 2017; Nilsson, 2021) and in models (Dong, 2014; Holmström and Wang, 2015; Regoli, 2018; Ma, 2019; Brecht, 2017).

Both measurements and models have limitations when applied to study the escape of ionospheric ions. For the detection by instruments on spacecrafts, it's difficult to cover all energies, especially low energies, and the full 4π sr field of view. Further-

35 more, an in-situ observation is only at a certain place and time. To cover all of the interaction region, we need to accumulate data for a long time and rely on statistics. Therefore, observing the complete interaction region at a specific time is impossible with a single spacecraft. Using simulations, we can get a full three-dimensional picture at any instance. Nevertheless, the atmosphere are highly dynamic and it's impossible to include all relevant physics in the models. Therefore, we here use a recently proposed method to take advantage of both measurements and models, to get a global coverage of data and to enable detailed

40 studies of physical processes.

We use the amount of mass-loading of the solar wind as a free parameter to combine the model and observations. Mass-loading of the solar wind flow occurs wherever thermal ions are inserted into the flow. Mass loading by planetary ions slows down the solar wind and raises the bow shock (Alexander and Russell, 1985; Vignes, 2002; Mazelle, 2004; Hall, 2016). Given similar upstream conditions, the standoff distance of the bow shock from the planet will depend on the degree of mass-loading, which

45 is dependent on the amount of ions in the upper parts of the ionosphere. At Mars, heavy ions at the top of the ionosphere will provide the mass-loading, and wave-particle interactions will generate a bow shock in the colissionless solar wind plasma upstream of the planet (Szegö, 2000). We use observed upstream solar wind parameters as input for a hybrid plasma model, where the total ion upflux at the exobase is a free parameter. We then vary this ion upflux to find the best fit for the observed bow shock location. A motivation for having such a simplified ionosphere, represented by only one free parameter, is that the

50 ionosphere is highly variable in time and space (Chaufray, 2015; Fowler, 2022; Leelavathi, 2023), making the construction of an accurate ionospheric model difficult.

The method was introduced by Holmström (2022). The model used in that work was simplified, where only protons were considered in the solar wind, solar wind velocity aberration was not included and only one heavy ion specie was implemented in the ionosphere. Here we use a three-species ionosphere (O^+, O_2^+, CO_2^+), a solar wind with alpha particles and velocity

55 aberration. Using this improved model, we investigate the effects of including these parameters in the model, in particular ion composition, on the escape and morphology.

2 Model implementation

2.1 Model description

In a hybrid model, electrons are treated as a massless fluid and ions are treated as individual particles accelerated by the Lorentz
60 force (Holmström, 2022). The electric field is given by

$$\boldsymbol{E} = \frac{1}{\rho_I}(-\boldsymbol{J}_I \times \boldsymbol{B} + \mu_0^{-1}(\nabla \times \boldsymbol{B}) \times \boldsymbol{B} - \nabla p_e) + \frac{\eta}{\mu_0}\nabla \times \boldsymbol{B}, \tag{1}$$

where $\boldsymbol{B}$ is the magnetic field, ρ_I is the ion charge density, $\boldsymbol{J}_I$ is ion current density, p_e is the electron pressure, η is the
resistivity and μ_0 is the vacuum permeability, respectively. Faraday's law is used to advance the magnetic field in time by

$$\frac{\partial \boldsymbol{B}}{\partial t} = -\nabla \times \boldsymbol{E} \tag{2}$$

65

We use Mars Solar Orbital (MSO) coordinates, where the origin is at the center of the planet, the X_{MSO}-axis is directed to
the sun, the Y_{MSO}-axis is in the orbital plane, perpendicular to the X_{MSO}-axis, and opposite to Mars' motion. Then Z_{MSO}-
axis completes the right-handed coordinate system. Our simulation domain is -11000 km $\leq X_{MSO} \leq$ 10000 km, -34300 km
$\leq Y_{MSO}, Z_{MSO} \leq$ 34300 km and the cell size is $h =$350 km. We have a spherical obstacle centered at the origin with a radius
70 of 3550 km, representing the exobase. All ions inside the obstacle are removed from the simulation. The resistivity is $7 \cdot 10^5$ Ωm
in a sphere of radius 3380 km representing the solid planet. Outside the planet the resistivity is $5 \cdot 10^4$ Ωm, in the ionosphere and
the surrounding plasma. The vacuum regions are defined as the regions with a plasma density less than 1% of the solar wind
density and the resistivity in vacuum regions is 10^6 Ωm. The number of macro particles per cell at the inflow boundary (the
$+X_{MSO}$ side of the simulation box) is 8 for protons, and 2 for alpha particles. The weight (number of real particles represented
75 by one macro particle) of the ionospheric ion macro particles are set to the same weight as for protons. The time step, Δt, is
0.2 s. The heavy ions are produced on the dayside, drawn from a Maxwellian distribution with a temperature of 200 K. The
exobase ion upflux decays from the the subsolar point to the terminator by the cosine of solar zenith angle (Holmström and
Wang, 2015). Each produced heavy ion is then moved radially outward by a distance randomly drawn from $[0, h]$. We run the
model until a steady state is reached, after approximately 500 seconds of simulation time (when the number of heavy ions
80 in the simulation domain remains on average constant). We do not include any neutral corona in the model. We can however
note that in our method, additional mass loading from photoionization of neutrals in the exosphere will be compensated for by
larger heavy ion upflux at the exobase, to achieve the observed bow shock location.

We apply observed upstream solar wind parameters (solar wind density, velocity, ion and electron temperatures, and magnetic
field) at the inflow boundary. To derive these parameters, we calculated their median values of the undisturbed solar wind
85 with MAVEN Key Parameters file outside the nominal bow shock (Vignes, 2000). Then we run several simulations with
different heavy ion upflux rates at the exobase. Next, we compare the simulation results with observations in magnetic field
and the proton density, to find the simulation run that best fits the observed bow shock location. The space resolution of these

Table 1. Upstream solar wind parameters in MSO coordinates from 13:00 to 15:00 on 1 March 2015 estimated from MAVEN observations

Density [cm^{-3}]	2.4
Velocity [km/s]	(-350, 45, 12)
Proton temperature [K]	1.2×10^5
Electron temperature [K]	1.7×10^5
Interplanetary magnetic field [nT]	(-1, -2.7, -1)

Table 2. The total exobase ion upflux and resulting total escape rates used for the three simulations

Case	O$^+$ [s^{-1}]	O$_2^+$ [s^{-1}]	CO$_2^+$ [s^{-1}]	Escape rate [s^{-1}]
Upflux 1	4.6×10^{24}	3.2×10^{24}	6.1×10^{23}	5.08×10^{24}
Upflux 2	5.0×10^{24}	3.6×10^{24}	6.7×10^{23}	6.78×10^{24}
Upflux 3	5.5×10^{24}	3.9×10^{24}	7.3×10^{23}	8.94×10^{24}

observations is higher than of model. We can then derive an escape rate estimate from this best fit run. The total escape rate is computed by averaging the outflow in the region $X_{MSO} < -1.5 R_m$ over 500 s to 600 s simulation time with 30 s interval.

2.2 Model example

In this study, we apply our method to one reference orbit from 13:00 to 15:00 UTC on 1 March 2015. Table 1 displays the upstream solar wind conditions for this orbit from MAVEN observations. We run three simulations with three different total exobase upflux rates listed in Table 2. All the runs are with the same input upstream conditions listed in Table 1, and with 5% number density of alpha particles (same upstream temperature and velocity as for protons) and with an exobase upflux composition of 54% O$^+$, 39% O$_2^+$ and 7% CO$_2^+$, which will be discussed later. The simulation results are then compared with MAVEN measurements of magnetic field, solar wind velocity and proton density in Fig 1.

By visual inspection, the Upflux 2 simulation fits the observation best. Upflux 1 gives a bow shock too close to the planet, since the mass loading is too small, while Upflux 3 gives a bow shock too far away from the planet. We see a good agreement between the model and observations in the magnetosheath region (the grey area in Fig 1). While closer to the planet, below the Induced Magnetosphere Boundary (IMB), the model magnetic field is not increasing as much as in the observation, but we do not expect a perfect fit due to the simplified ionosphere we use, and the lack of crustal magnetic fields in our model. We also verify the fit for the Upflux 2 simulation using MEX Electron Spectrometer (ELS) observations of bow shock crossings in Fig 2. This supports that Upflux 2 is the best fitting simulation run. In the rest of this work, we use this simulation as a reference.

3 Results and discussions

In what follows, we investigate the effects of alpha particles, heavy ion composition, velocity aberration, and solar wind electron temperature on escape estimates. We then study in what regions near the planet that ions escape.
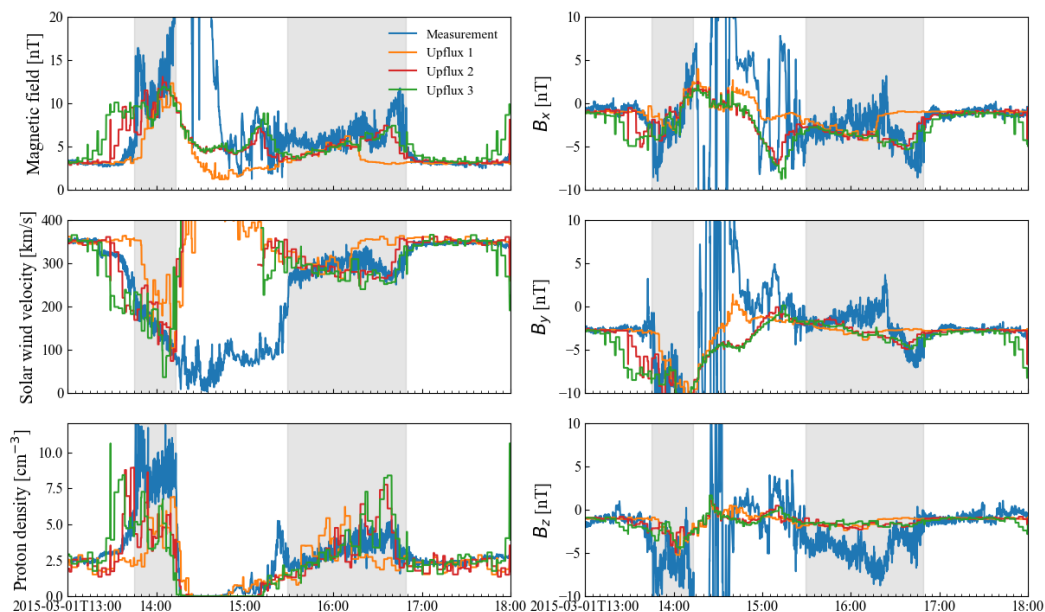
Figure 1. Model results compared to MAVEN measurements (blue lines). Orange, red and green lines are the simulation results for three different productions in Table 2, respectively. The left column shows a comparison for the magnetic field magnitude, the solar wind velocity and the proton density. The right column shows the three components of the magnetic field. The bow shock location is identified by the change in magnetic field and solar wind density. The grey areas indicate the magnetosheath regions.
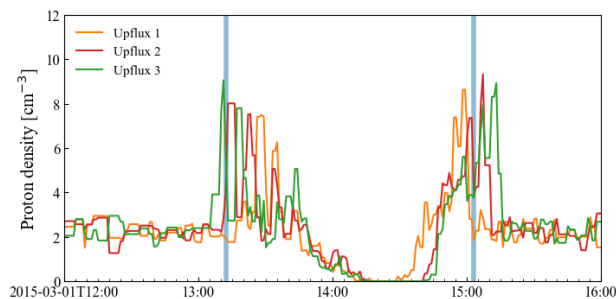
Figure 2. Model results of Table 2 compared to MEX measurements. Blue lines are bow shock crossing times identified from MEX ELS observations.

3.1 Effects of parameters on escape estimates

3.1.1 Effects of alpha particles on escape estimates

In addition to protons and electrons, the upstream solar wind contains a variable amount of alpha particles, He^{++}. Upstream

110 solar wind observations from the Solar Wind Ion Analyzer (SWIA) on MAVEN suggests a 3%-5% abundance of alpha particle populations in number density (Halekas, 2017). Despite the low percentage, alpha particles carry up to $\sim$20% of the solar wind kinetic energy due to its mass. Therefore, including alpha particles in the model will increase the kinetic energy density and dynamic pressure of the solar wind, thus impacting the solar wind interaction with Mars.

Furthermore, previous studies found that the alpha temperature is higher than the proton temperature and their ratio changes

115 with heliocentric distance (Marsch, 1982; Von Steiger, 1995; Araneda, 2009; Hellinger, 2013) since the solar wind particles encounter parallel cooling and perpendicular heating driven by kinetic and Alfvén-cyclotron wave instabilities and heavier ions are preferentially heated (Araneda, 2009; Hellinger, 2013). At 1 AU, the ratio between alpha temperature (T_α) and proton temperature (T_p) has been observed to vary from 2.5 to 5 (Bourouaine, 2011; Wilson, 2018; Stansby, 2019).

We now investigate how our ionospheric heavy ion escape rate estimates are affected by alpha particle abundance and temper-

120 ature in the solar wind. We ran two more cases in addition to the reference case with Outflow 2 in Section 2.2, which is Case 2, the baseline case, in this exercise. In Case 1, we only include protons. In Case 3, we increase the alpha temperature to 5 times that in Case 2. We keep the total solar wind particle number density (sum of protons and alpha particles) the same. In Cases 2 and 3, the upstream solar wind contains 5% alpha particles. All the relevant parameters are listed in Table 3. The total exobase ion upflux used in these cases can be found in Table A.1.

125 We find that the model escape rate estimate is slightly higher when we include alpha particles in the upstream solar wind (Case 2 in Table 3) than when we exclude them (Case 1 in Table 3). This is probably because including the heavier alpha particles increases the dynamic pressure of the upstream solar wind, since we keep the total number density of the solar wind constant. The increased dynamic pressure requires a larger exobase upflux to keep the bow shock at the same location, hence increasing the escape.

130 To examine the effect of alpha temperature on ion escape in our method, we used $T_\alpha = 5T_p$ for comparison with the case of identical temperature for protons and alpha particles (Case 2 in Table 3). Hotter alpha particles (Case 3 in Table 3) with larger thermal pressure compress the bow shock more, which requires an increased mass loading (from larger inner boundary heavy ion upflux). This finally leads to 3% more escape. Considering this small increase and the lack of knowledge of actual alpha temperature around Mars, later in this study, we keep the alpha particles temperature the same as for protons.

135 #### 3.1.2 Effects of heavy ion composition on escape estimates

The heavy ion composition of the upper parts of an ionosphere directly influences the composition of escaping plasma, as well as the dynamics of the escaping plasma due to their different mass per charge ratios. It is therefore important what composition of different ion species that we use in our model's exobase ion upflux. Carlsson (2006) found that O^+ is the most abundant escaping species. They measured a flux ratio of $O^+/O_2^+/CO_2^+ = 10:9:2$ inside the IMB using MEX Ion Mass Analyser (IMA)

Table 3. Parameters used for the simulation runs investigating the effects of alpha particle, and the resulting escape estimates.

Simulation Cases	Proton density [cm^{-3}]	Alpha density [cm^{-3}]	Alpha temperature	Escape rate [s^{-1}]
Case 1	2.4	0	0	6.44×10^{24}
Case 2 (baseline)	2.28	0.12	$T_\alpha = T_p$	6.78×10^{24}
Case 3	2.28	0.12	$T_\alpha = 5T_p$	6.98×10^{24}

140   nightside data. With the same instrument, Rojas (2018) found a number ratio of O$^+$/O$_2^+$ = 1.3 averaged over the whole space inside the IMB. Inui (2019) discovered larger O$_2^+$ flux than O$^+$ in the wake region based on MAVEN observations. In summary, the measurements show uncertainties in the composition of escaping ions. Therefore it's of interest to explore the influence of different heavy ion compositions on escape estimates. In our model, we specify the ratio between the different species, in addition to the total upflux, to fit the bow shock location. Here we consider O$^+$, O$_2^+$, and CO$_2^+$ since those are the major

145   observed ion species, and the ones typically considered in models of the interaction between Mars and the solar wind (Kallio, 2008; Ma, 2014; Holmström and Wang, 2015).

In Fig 3, we present escape rates of seven different O$^+$/O$_2^+$ ratios of the total exobase upflux. We examine the O$^+$/O$_2^+$ ratio because O$^+$ and O$_2^+$ are the most abundant heavy ion species at Mars (Carlsson, 2006; Rojas, 2018; Inui, 2019). The total exobase ion upflux, and composition, used in all simulation runs in this paper can be found in Table A.1. In every case, we

150   adjust the total upflux rate to fit the observed bow shock location. As the O$^+$ upflux fraction increases from 0 to 100%, the total escape rate increases by 45%. So the escape is not inversely proportional to the mass of the escaping ion specie. In that case we would have an increase of 100%. Instead, the ratio of the escape for the cases of only O$^+$ exobase upflux and only O$_2^+$ upflux is close to $\sqrt{2} \approx 1.41$, suggesting that escape scales inversely with the square root of the atomic mass of the escaping ion specie. To test this hypothesis, we made an unrealistic run with only CO$_2^+$ exobase upflux, resulting in an escape estimate that is 58%

155   smaller than the O$^+$ case. This value is close to inverse of the square root of the mass ratio, $\sqrt{44/16} \approx 1.66$, supporting the scaling hypothesis. It is not surprising that we do not have a perfect scaling when comparing the escape rates of the different species, since the escape process should not only have a dependence on the mass of different species, but will also be affected by the different trajectories due to differences in the mass per charge of the species.

We can here only speculate as to why escape rates would scale inversely with the square root of the atomic mass of the escaping

160   ion specie. Since flux is proportional to velocity, that in turn is proportional to the square root of kinetic energy divided by mass, we would have an inverse dependence on square root of mass. Assuming that the kinetic energy is constant. So maybe the total energy flux of the escaping ions is similar, independent of the species of the escaping ions. This would mean that the same power is transfered from the upstream solar wind to the escaping ions. It also seems reasonable that the same power is required to keep the bow shock at the same distance.

165   We can note that there is only a 5% increase in escape as O$^+$ increases from 48% to 68%, indicating that the escape estimate is not so sensitive to the exact O$^+$/O$_2^+$ ratio of the exobase upflux. Therefore, we use 54% O$^+$, 39% O$_2^+$ and 7% CO$_2^+$ as the composition of the exobase upflux hereafter.
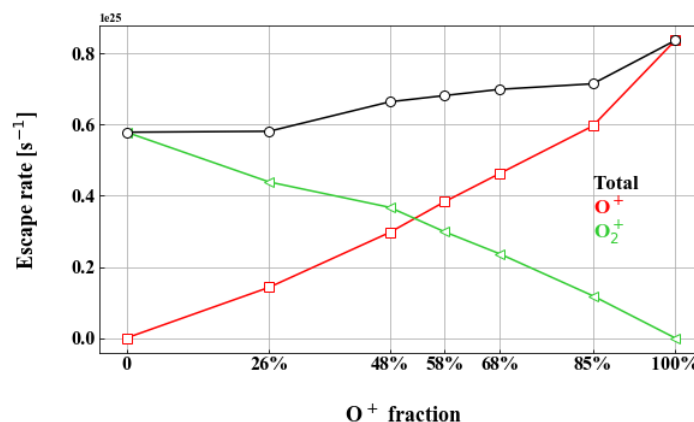
Figure 3. Escape rate for different compositions of the ion upflux at the exobase (inner boundary). The red line represents O^+ escape rate. The green line represents O_2^+ escape rate. The black line represents total escape rate. The O^+ fraction is of the total exobase number upflux, where the rest is O_2^+ in this experiment.
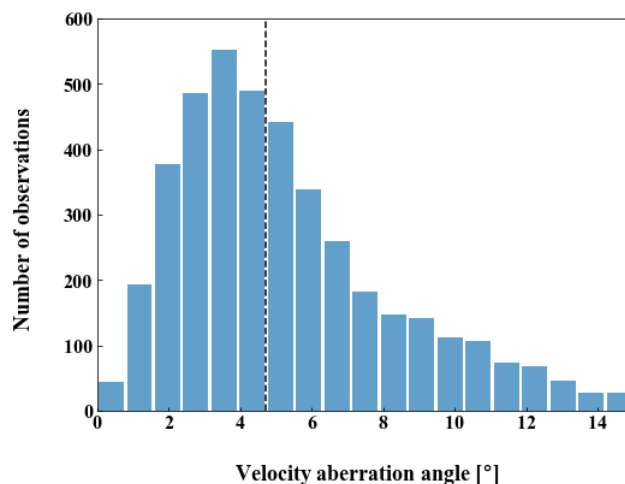
Figure 4. Velocity aberration distribution calculated from MAVEN SWIA solar wind observations during 2014-2019. The median velocity aberration angle ($4.7°$) is marked by a black dashed line.

3.1.3 Effects of solar wind velocity aberration on escape estimates

Velocity aberration is the deviation of the upstream solar wind velocity direction from the anti-sunward direction ($-X_{MSO}$). It
170   is due to the planet's orbital motion around the Sun, and disturbances in the solar wind. At Venus the orbital velocity is around 35 km/s (Lundin, 2011, 2013), and possibly causes O^+ flow asymmetry in the plasma tail (Lundin, 2011) and large-scale flow vortex (Lundin, 2013). At Mars, the typical aberration angle is approximately $5°$ and usually ignored (Halekas, 2017a) for the

tenuous and less viscous atmosphere.

In our model, the solar wind aberration is included since we use the upstream solar wind proton velocity vector observed by
175 MAVEN. However, it is of interest how much variations of this angle affect the Mars-solar wind interactions since it is not
completely stable in the upstream solar wind, and accurate velocity vectors are not always available. The aberration introduces
an asymmetry since the ionosphere in the model is still symmetric around the X_{MSO}-axis. Here we investigate the effects of
aberration on the heavy ion escape and on the global solar wind interaction.

MAVEN can observe the full solar wind velocity vector. Examining 4117 orbits of SWIA data from November 2014 to Novem-
180 ber 2019, we compute a velocity aberration distribution (Fig 4). The median velocity aberration angle is $4.7°$. In some cases,
it is up to $15°$. The solar wind velocity aberration angle of the orbit we used in this paper is $7.6°$. For comparison, we run
two more simulations in addition to the baseline case (Case 6, the same as Case 2 with Upflux 2 in Section 2.2). In Case 4 we
assume solar wind travels along $-X_{MSO}$ without velocity aberration. When we change the solar wind velocity direction, the
IMF cone angle (angle between solar wind velocity and the IMF) should rotate simultaneously to keep the same magnitude
185 of the convective electric field. So in Case 5, with no velocity aberration, we have also rotated the IMF to keep the IMF cone
angle the same as Case 6.

In Table 4, we see the effects of different velocity aberrations on escape. When we assume no aberration (Case 4), the escape
increases by 7% (compared to Case 6). When we rotate the upstream IMF to keep the cone angle the same (Case 5), the differ-
ence in escape (compared to Case 6) is only 1%. The conclusion is that the largest effect from different assumed aberrations is
190 the different angles between the upstream solar wind velocity and the magnetic field, resulting in different upstream convective
electric fields. The effect of having the upstream solar wind velocity at an angle relative to the ionosphere is minor in compar-
ison.

However, the effect of having the solar wind at an angle to the symmetry axis of the ionosphere (the X_{MSO}-axis) should be
larger at further distances in the tail behind the planet, since it represents a tilt of the whole induced magnetosphere. In Fig. 5
195 we examine this by looking at a plane at $X_{MSO} = -1.5R_m$ down the tail. We see that the morphology of the central heavy
ion fluxes are quite different. The maximum flux is distributed in different regions in three cases. Case 4 has the maximum
flux on both $+Y_{MSO}$ side and $-Y_{MSO}$ side. In case 5, large flux is widely distributed in the margin. While in Case 6, most of
the flux is concentrated on $+Y_{MSO}$ side. The direction of the plume flux is also different. Small differences are magnified as
we go further distances down the tail. The rotation of the magnetosphere is visible comparing Case 5 and 6, where the plume
200 direction is visibly tilted.

In conclusion, the effect of velocity aberration is a tilt of the whole magnetosphere, so that the line of symmetry of the mag-
netosphere is along the upstream flow direction instead of the X_{MSO}-axis. This effect will be larger further behind the planet.
If the angle between the upstream magnetic field and velocity remains the same, the effects on the interaction (except for the
tilt) will be small. If however this angle change, it will affect the global interaction, probably due to the change in the upstream
205 convective electric field.

Table 4. Parameters used for the simulation runs investigating the effects of velocity aberration, and the resulting escape estimates.

Simulation Cases	Velocity [km/s]	IMF [nT]	Escape rate [s^{-1}]
Case 4	(-353, 0, 0)	(-1, -2.7, -1)	7.27×10^{24}
Case 5	(-353, 0, 0)	(-0.6, -2.1, -2.1)	6.88×10^{24}
Case 6 (baseline)	(-350, 45, 12)	(-1, -2.7, -1)	6.78×10^{24}

Heavy ions flux at X$_{MSO}$ = -1.5R$_m$, [m^{-2}s^{-1}]

ions1.png
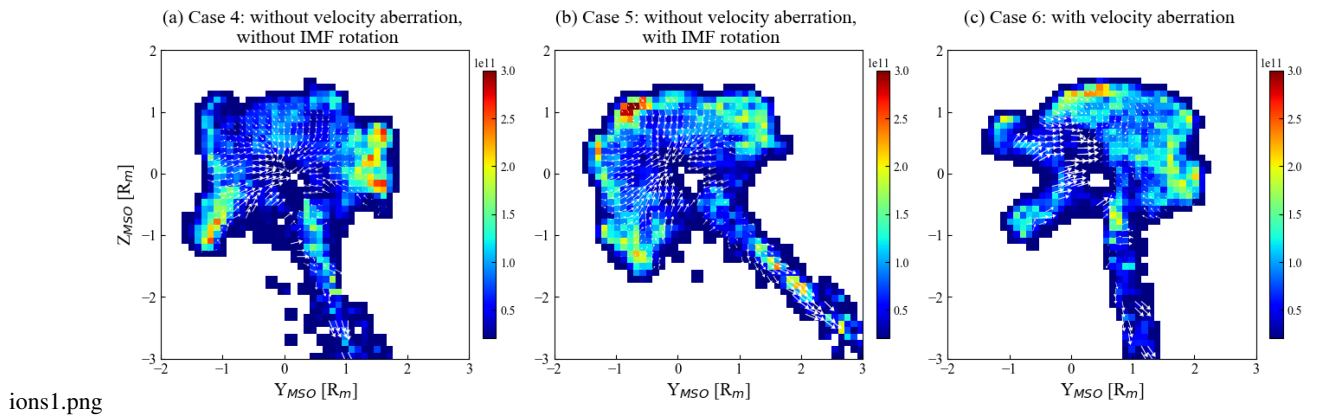
Figure 5. The panels show the heavy ions flux in $Y_{MSO} - Z_{MSO}$ plane sliced at $X_{MSO} = -1.5R_m$ of three cases decribed in Table 4. The white arrows denote the direction of flux. The length of arrows show the velocity magnitude, with larger velocities in the energetic plume region.

3.1.4 Effects of electron temperature and ambipolar field on escape estimates

The ambipolar field plays a role in the solar wind interaction with Mars by enhancing ion loss in the collisionless ionosphere above the exobase (Ergun, 2016; Brecht, 2017; Ma, 2019). In the upper Martian atmosphere, lighter electrons diffuse faster than ions and an electric field is generated in the direction against the density gradient, called the ambipolar field. Ergun (2016) showed increased O_2^+ outflow with increasing high-altitude electron temperature. Xu (2021) utilized electrostatic potential from MAVEN measurements (Xu, 2021a; Horaites, 2021) to estimate the global ambipolar field at Mars, which agrees well with MHD model predictions (Ma, 2019).

The ambipolar field cannot be self-consistently represented in MHD and hybrid models due to the assumptions of charge neutrality. There are different approaches of how to include the effects of the ambipolar electric field in the models. It is therefore of interest to look at how the ambipolar field is approximated in a hybrid model. The ambipolar field in our model is derived from the gradient of the electron pressure, $p_e = n_e k T_e$. Thus our ambipolar field is related to the electron temperature.

In our model, the electron pressure is isotropic and computed from the charge density by (Holmström, 2010)

$$\frac{p_e}{p_{e0}} = \left(\frac{\rho_e}{\rho_{e0}} \right)^\gamma \tag{3}$$

where $\gamma = 5/3$ is the adiabatic index, p_{e0} and ρ_{e0} the electron pressure and electron charge density in the upstream solar wind,
220 where $p_{e0} = n_{e0} k T_{e0}$. k is the Boltzmann constant and T_{e0} is the solar wind upstream electron temperature. Here we get

$$p_e = A \rho_e^\gamma \quad \text{with} \quad A = \frac{k}{m_e} T_{e0} \rho_{e0}^{1-\gamma} \tag{4}$$

where $\rho_e \equiv \rho_I$ and $\rho_{e0} \equiv \rho_{I0}$ for charge neutrality. Since the ambipolar term in Equation (1) is calculated from the negative gradient of the electron pressure, this electric field will be largest in regions where the total charge density has the largest gradient.

225 Fig 6 shows the electron pressure and the ambipolar electric field. The ambipolar field is largest at two boundaries, the bow shock and, closer to the planet, the IMB. The magnitude of our ambipolar field is up to 0.1 V/km at the boundaries. At the topside of the Martian ionosphere (dark red region closed to planet in Fig 6), the ambipolar field energizes O^+, O_2^+ and CO_2^+ with accelerations of nearly 0.6, 0.3 and 0.2 km/s^2, which can lead to the heavy ions escaping (Kar, 1996). The black arrows in Fig 6 (d), (e), and (f) show the direction of the ambipolar field. The field points outwards at both boundaries. At the bow shock,
230 the ambipolar field direction is consistent with MAVEN observations (Figure 2 in Xu (2021)) and MHD model results (Figure 3 in Xu (2021)). On the IMB, the ambipolar field in our model is directed outward while some observations suggest however that the field is directed inward in that region due to the electron pressure gradient from the colder ionosphere to the hotter magnetosheath (Xu, 2021). The reason for this discrepancy might be that as is common in hybrid models we use an adiabatic approximation for the electron pressure term. This means that the resulting ambipolar field term will be directed opposite to
235 charge density gradients. The electron temperature, and thereby the electron pressure, is a free parameter in hybrid models. Electron density and current is given from quasi-neutrality and Ohm's law, respectively. It would be of interest in future work to study in detail alternatives to the adiabatic approximation. One approach taken is to assume an electron temperature profile in the ionosphere (Bößwetter, 2004; Modolo, 2016). Another approach is to solve a fluid flow equation for the electrons (Brecht, 2017).

240 To test the sensitivity of the escape rate to changes in the upstream electron temperature, we run three cases with different upstream electron temperatures (the minimum, the median and the maximum temperature observed in the undisturbed solar wind) but with other parameters the same. The results are shown in Figure 7. We see that the escape rate is sensitive to the assumed upstream electron temperature and increases with it, probably because the larger electron temperature leading to a larger ambipolar field accelerates more ions to escape energies. Since we use the observed upstream electron temperature in
245 our model, this is not a problem, except for measurement uncertainties. However, it indicates that escape estimates are sensitive to the model assumptions regarding the ambipolar fields. The effects of different approaches to include the effects of charge separation in a hybrid model, and how it affects model results, would be a topic of future studies.
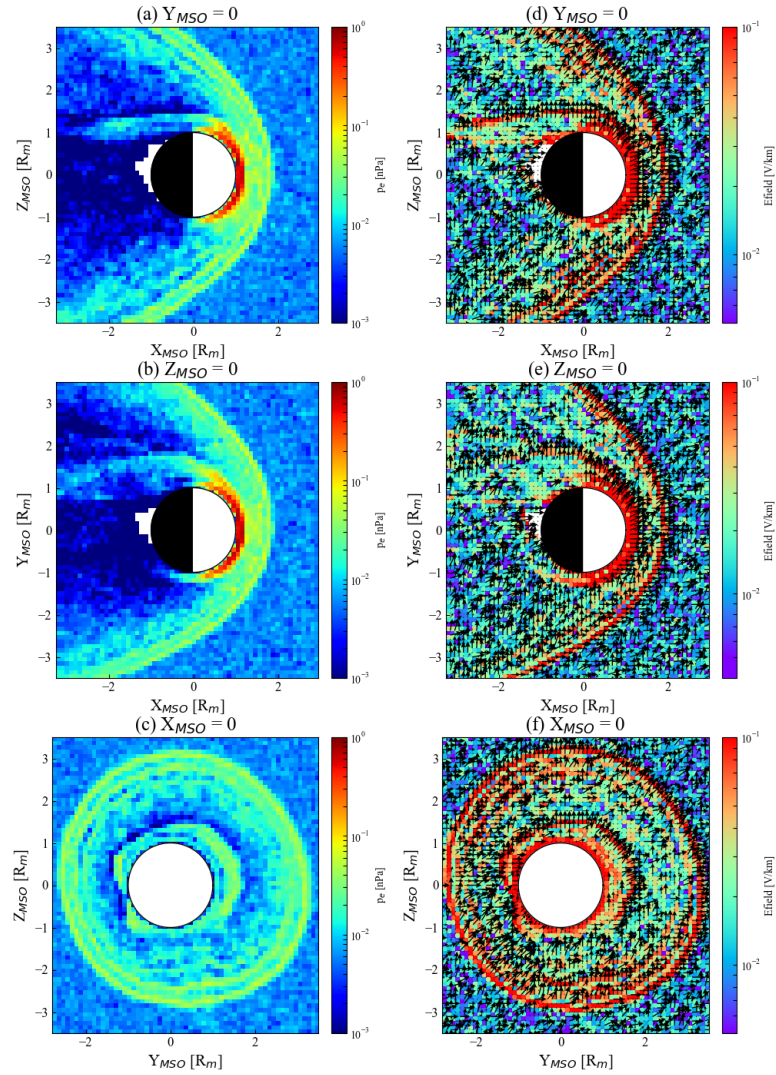
Figure 6. Electron pressure (a), (b), (c) and ambipolar electric field (d), (e), (f) from hybrid model. (a) and (d) is in $X_{MSO} - Z_{MSO}$ plane at Y_{MSO}=0. (b) and (e) is in $X_{MSO} - Y_{MSO}$ plane at Z_{MSO}=0. (c) and (f) is in $Y_{MSO} - Z_{MSO}$ plane at X_{MSO}=0. Black arrows in (d), (e) and (f) represent the direction of ambipolar electric field in each plane.
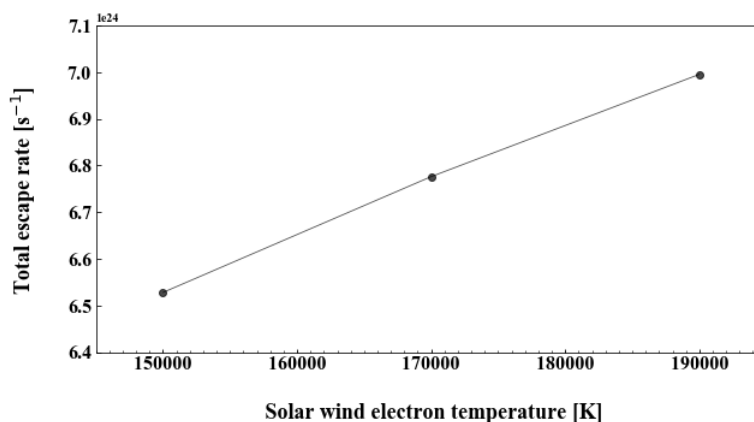
Figure 7. The total escape rate of three tests with various electron temperatures. The electron temperature in the middle (1.7×10^5 K) is the median value of the undisturbed upstream solar wind and is what we used elsewhere in this study. 1.5×10^5 K and 1.9×10^5 K are the minimum and maximum values in the undisturbed solar wind from observations.

3.2 Morphology of heavy ions escape

Our method of combining observations and modeling gives us a self-consistent description of the Mars-solar wind interaction,
250 which can be used to study other properties of the solar wind interaction than escape. We now examine the morphology of the escaping ions, using the exobase upflux ion composition of 54% O^+, 39% O_2^+ and 7% CO_2^+. In the upstream solar wind we have 5 % solar wind alpha particles, with the same temperature as protons, as discussed before.

At Mars the escaping ionospheric ions usually form two major outflow channels: A cold fluid-like outflow in the tail behind the planet, and a more energetic outflow in the direction of solar wind convective electric field (Holmström and Wang, 2015). The
255 escaping ions accelerated by the convective electric field $-\mathbf{V}_{SW} \times \mathbf{B}$, are usually called the ion plume at Mars. The Martian ion plume has been observed by MAVEN (Dong, 2015, 2017; Dubinin, 2017) and MEX (Nilsson, 2021), and modeled by multifluid MHD (Dong, 2014; Regoli, 2018; Ma, 2019) and hybrid codes (Holmström and Wang, 2015; Brecht, 2017). It is a matter of definition how to separate tail and plume fluxes, in observations and models. Dong (2017) separated plume and tail flux by energy (>1 keV ions belong to the plume) and found that plume escape contributes 30% to total escape in low EUV
260 conditions and 20% in high EUV conditions. Nilsson (2021) defined the escape morphology using geometric box and called the outflow perpendicular to the X-axis "radial escape". They found that the radial escape does not depend on the solar cycle, but that the highest radial escape occurs at highest solar wind dynamic pressure conditions, and that the radial escape is around 20% to 40% of the total escape. Previous studies show that the amount of plume and radial escape, as a fraction of total escape, is not very sensitive to the exact definition chosen.
265 To separate escaping ions into plume and tail, we define a three-dimensional box in the simulation domain with a size similar to Nilsson (2021) and Dong (2017). Our box is defined by $X_{MSO} = \pm 1.6$ R_m and $Y_{MSO}, Z_{MSO} = \pm 1.7$ R_m. Using a +1.6 R_m as the boundary in the $+X_{MSO}$ direction instead of +2 R_m used in other studies (Dong, 2017; Nilsson, 2021) will not
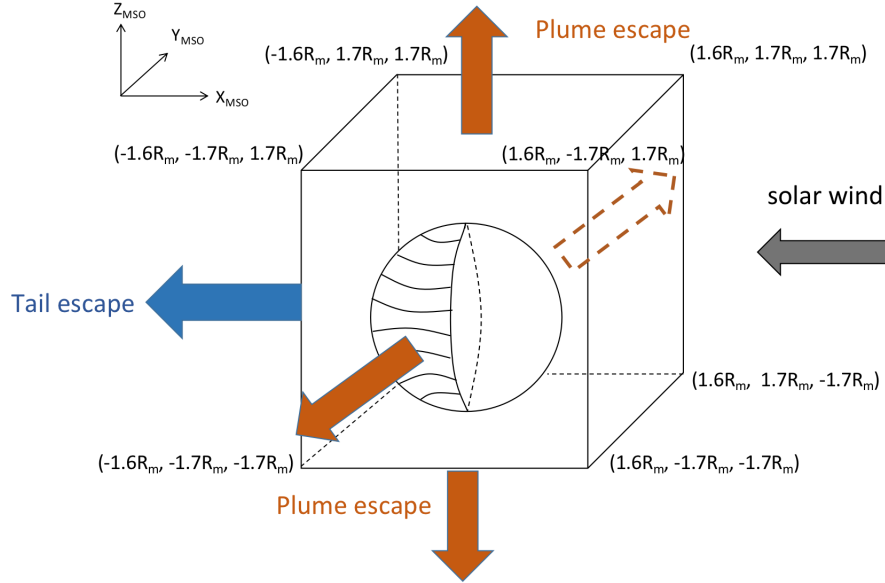
Figure 8. Illustration of how plume and tail escape is defined in this study. The flux passing through the $Y_{MSO} - Z_{MSO}$ side of the box along $-X_{MSO}$ we define as tail flux (the blue arrow). The flux passing through the $X_{MSO} - Z_{MSO}$ and $Y_{MSO} - Z_{MSO}$ sides of the box is defined as plume flux (the orange arrows). The direction of the convective electric field determine the direction of the plume flux.

Table 5. The percentage for each ion specie in tail escape, plume escape and total escape, in terms of number of ions.

Ion specie	Tail	Plume	Total
O^+	58%	37%	51%
O_2^+	36%	51%	41%
CO_2^+	6%	12%	8%
All	100%	100%	100%

affect our results since there is little heavy ion flux beyond $X_{MSO} = +1.6$ R$_m$. We define the outward ion fluxes through the $\pm Y_{MSO}$ and $\pm Z_{MSO}$ sides of the box as the plume flux and the fluxes through the $-X_{MSO}$ side as the tail flux (Fig 8). The
270 thickness of the cross section of every side is one layer of cell size (350 km).

Fig 9 displays our model results of Case 2 in Table 3 for the flux of the three heavy species in three of the planes. The first row in Fig 9 displays the tail flux and the second and third rows display the plume flux. We obtain a plume escape rate of 1.96×10^{24} s^{-1}, accounting for 29% of the total escape. This number is close to the observation results discussed above and a bit lower than MHD model results (35% to 45%) (Regoli, 2018). Table 5 illustrates that O^+ escape is dominant in the total and
275 tail escape. O_2^+ is dominant in the plume escape. Higher O_2^+ composition in plume could be due to the fact that heavier ions, with larger gyro radius, easier to escape as plume since the flow is more perpendicular to the X_{MSO}-axis.
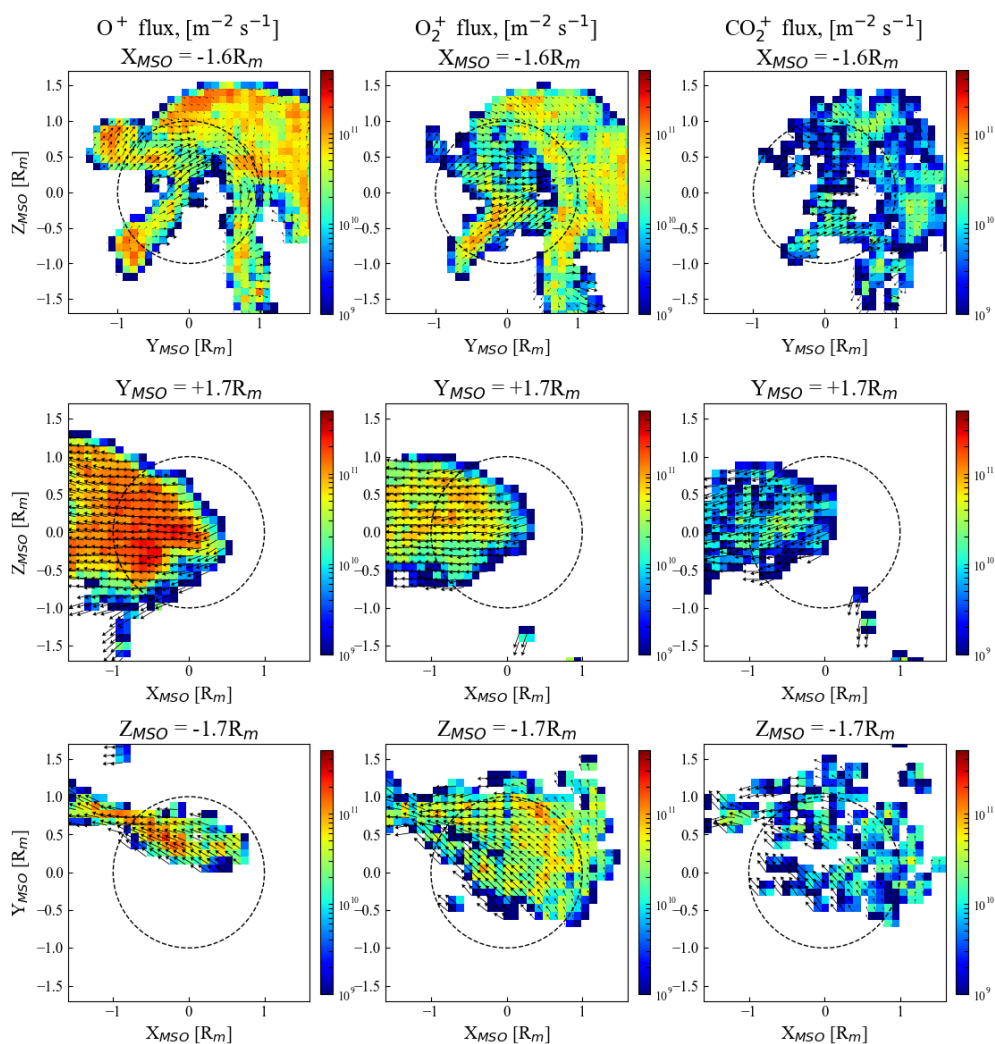
Figure 9. The distribution of the tail and plume flux divided according to Figure 8. The leftmost column shows O^+ flux, the middle column O_2^+ flux, and the rightmost column CO_2^+ flux. The first row show tail flux, and the two lower rows show plume flux. The black arrows indicate the direction of the flux. Notice that for this simulation there is no plume flux through the $-Y_{MSO}$ or $+Z_{MSO}$ sides.

4   Conclusions

We have improved a new method for modeling the interaction between the solar wind and Mars, which uses a hybrid model to fit the observed bow shock location to determine a corresponding exobase ion upflux. The method was applied to one MAVEN orbit #811 on 2015-03-01, to investigate the effects on ion escape estimates of assumed heavy ion composition in the ionosphere, alpha particles in the solar wind, solar wind velocity aberration and electron temperature. We also studied ion escape rate in the plume and in the tail of the planet.

1. We find that ion compositions at the exobase with larger mass leads to a smaller estimate of the escape rate. The escape estimate is inversely proportional to the square root of the atomic mass of the escaping ion specie. However, the escape does not change substantially as the mixing ratio of O^+ relative to O_2^+ varies between 0.4 and 0.6, the range of observed composition of heavy ion fluxes.

2. We also find that the assumed fraction, and temperature, of alpha particles in the upstream solar wind, have a small effect on escape estimates. The escape increase by 5% when having a number fraction of 5% alpha particles in the upstream solar wind. Adding alpha particles increases the mass density of the upstream solar wind, compressing the bow shock. We then need a larger mass loading from heavy ion upflux at the exobase, resulting in larger escape. This was the case when the temperature of the upstream protons and alpha particles were assumed to be equal. If we assume a five times alpha temperature, we see a further 3% increase in escape due to the higher thermal pressure in the upstream solar wind further compressing the bow shock.

3. The effect of solar wind aberration on escape rate is found to be 7%. This is however when only rotating the upstream solar wind velocity. If we also rotate the upstream magnetic field we find a change of only 1%. So the major effect is from having a different angle (cone angle) between the solar wind velocity and the IMF. The minor effect is from having the upstream solar wind impacting the ionosphere from a different direction than the anti-sunward direction.

4. We find that the escape rate is sensitive to the assumed upstream electron temperature and increases with it. This indicates a sensitivity to the model assumptions regarding the ambipolar fields. In our model we find ambipolar field strength at boundaries up to 0.1 V/km.

5. We also studied the amount of escaping ions in the plume and the tail and find that 29% of the ions escape in the plume, consistent with observations. We also find that the fraction of ions, relative to the total escape, escaping in the plume increase with the mass of the ion specie. Possibly due to kinetic effects due to larger gyro radius.

This paper improves on our recent-proposed method and studies the role of some basic parameters on ion escape estimates at Mars. Future studies will further explore how upstream solar wind conditions and planetary conditions affect estimates of Martian heavy ion escape.

Table A.1. The total exobase ion upflux [s^{-1}] and escape rate [s^{-1}] for all simulation runs.

	O$^+$	O$_2^+$	CO$_2^+$	O$^+$ escape rate	O$_2^+$ escape rate	CO$_2^+$ escape rate	Total escape rate
Case 1	4.6×10^{24}	3.2×10^{24}	6.1×10^{23}	3.24×10^{24}	2.69×10^{24}	5.1×10^{23}	6.44×10^{24}
Case 2	5.0×10^{24}	3.6×10^{24}	6.7×10^{23}	3.46×10^{24}	2.77×10^{24}	5.5×10^{23}	6.78×10^{24}
Case 3	5.1×10^{24}	3.6×10^{24}	6.8×10^{23}	3.56×10^{24}	2.86×10^{24}	5.6×10^{23}	6.98×10^{24}
Case 4	5.0×10^{24}	3.6×10^{24}	6.7×10^{23}	3.69×10^{24}	3.03×10^{24}	5.5×10^{23}	7.27×10^{24}
Case 5	5.0×10^{24}	3.6×10^{24}	6.7×10^{23}	3.54×10^{24}	2.80×10^{24}	5.4×10^{23}	6.88×10^{24}
Case 6	5.0×10^{24}	3.6×10^{24}	6.7×10^{23}	3.46×10^{24}	2.77×10^{24}	5.5×10^{23}	6.78×10^{24}
0% O$^+$	0	7.8×10^{24}	0	0	5.79×10^{24}	0	5.79×10^{24}
26% O$^+$	2.2×10^{24}	6.2×10^{24}	0	1.42×10^{24}	4.39×10^{24}	0	5.81×10^{24}
48% O$^+$	4.4×10^{24}	4.7×10^{24}	0	2.97×10^{24}	3.67×10^{24}	0	6.64×10^{24}
58% O$^+$	5.5×10^{24}	3.9×10^{24}	0	3.83×10^{24}	2.99×10^{24}	0	6.82×10^{24}
68% O$^+$	6.6×10^{24}	3.1×10^{24}	0	4.62×10^{24}	2.37a×10^{24}	0	6.99×10^{24}
85% O$^+$	8.8×10^{24}	1.6×10^{24}	0	5.96×10^{24}	1.19×10^{24}	0	7.15×10^{24}
100% O$^+$	1.1×10^{25}	0	0	8.37×10^{24}	0	0	8.37×10^{24}
100% CO$_2^+$	0	0	6.6×10^{24}	0	0	5.28×10^{24}	5.28×10^{24}

Appendix A

In Table A.1, we summarize the upflux, composition and resulting escape for all the simulation case in this paper.

Author contributions. QZ initiated the study, run MH's models, and wrote the paper. All co-authors contributed to the discussion and the
310   reviewing of the paper.

Competing interests. The authors declare that they have no competing interests.

Acknowledgements. This work was supported by The Swedish National Space Agency, Grant 198/19.
Computing resources used in this work were provided by the Swedish National Infrastructure for Computing (SNIC) at the High Perfor-
mance Computing Center North (HPC2N), Umeå University, Sweden. The software used in this work was in part developed by the DOE
315   NNSA-ASC OASCR Flash Center at the University of Chicago.
The ASPERA-3 electron data used, from the ELS sensor, is available in ESA's Planetary Science Archive (PSA) at ftp://psa.esac.esa.int/pub/mirror/MARS-
EXPRESS/ASPERA-3/MEX-M-ASPERA3-3-RDR-ELS-EXT5-V1.0/

The MAVEN data used in this work, ion data from the SWIA instrument and magnetic field data from the MAG instrument, is available in University of Colorado Boulder's Planetary Data System (PDS) at https://lasp.colorado.edu/maven/sdc/public/data/sci/kp/

References

Alexander, C. J., and Russell, C. T. (1985). Solar cycle dependence of the location of the Venus bow shock. Geophysical research letters, 12 (6), 369-371.

Araneda, J. A., Maneva, Y., and Marsch, E. (2009). Preferential heating and acceleration of particles by Alfvén-cyclotron waves. Physical review letters, 102 (17),175001.

Barabash, S., Fedorov, A., Lundin, R., and Sauvaud, J. A. (2007). Martian atmospheric erosion rates. Science, 315 (5811), 501-503.

Bourouaine, S., Marsch, E., Neubauer, F. M. (2011). On the relative speed and temperature ratio of solar wind alpha particles and protons: collisions versus wave effects. The Astrophysical Journal Letters, 728 (1), L3.

Brecht, S. H., Ledvina, S. A. and Jakosky, B. M. (2017). The role of the electron temperature on ion loss from Mars. Journal of Geophysical Research: Space Physics, 122 (8), 8375–8390.

Bößwetter, A., Bagdonat, U., T. andcMotschmann, and Sauer, K. (2004). Plasma boundaries at Mars: a 3-d simulation study. Annales Geophysicae. Copernicus GmbH , 22 (12), 4363-4379.

Carlsson, E., Fedorov, A., Barabash, S., Budnik, E., Grigoriev, A., Gunell, H., et al. (2006). Mass composition of the escaping plasma at Mars. Icarus, 182 (2), 320-328.

Chaffin, M. S., Deighan, J., Schneider, N. M., and Stewart, A. I. F. (2017). Elevated atmospheric escape of atomic hydrogen from Mars induced by high-altitude water. Nature geoscience, 10 (3), 174-178.

Chaufray, J. Y., Gonzalez-Galindo, F., Forget, F., Lopez-Valverde, A., M., Leblanc, et al. (2015). Variability of the hydrogen in the Martian upper atmosphere as simulated by a 3d atmosphere–exosphere coupling. Icarus, 245 , 282-294.

Dong, C., Bougher, S. W., Ma, Y., Toth, G., Nagy, A. F., and Najib, D. (2014). Solar wind interaction with Mars upper atmosphere: Results from the one-way coupling between the multifluid MHD model and the MTGCM model. Geophysical Research Letters, 41 (8), 2708-2715.

Dong, Y., Fang, X., Brain, D. A., McFadden, J. P., Halekas, J. S., Connerney, J. E., et al. (2015). Strong plume fluxes at Mars observed by MAVEN: An important planetary ion escape channel. Geophysical Research Letters, 42 (21), 8942-8950.

Dong, Y., Fang, X., Brain, D. A., McFadden, J. P., Halekas, J. S., Connerney, J. E. P., et al. (2017). Seasonal variability of Martian ion escape through the plume and tail from MAVEN observations. Journal of Geophysical Research: Space Physics, 122 (4), 4009-4022.

Dubinin, E., Fraenz, M., Pätzold, M., McFadden, J., Halekas, J. S., DiBraccio, G. A., et al. (2017). The effect of solar wind variations on the escape of oxygen ions from Mars through different channels: MAVEN observations. Journal of Geophysical Research: Space Physics, 122 (11), 11,285–11,301.

Ergun, R., Andersson, L., Fowler, C., Woodson, A. K., Weber, T. D., Delory, G. T., et al. (2016). Enhanced O_2^+ loss at Mars due to an ambipolar electric field from electron heating. Journal of Geophysical Research: Space Physics, 121 (5), 4668–4678.

Fang, X., Ma, Y., Brain, D., Dong, Y., and Lillis, R. (2015). Control of Mars global atmospheric loss by the continuous rotation of the crustal magnetic field: A time-dependent MHD study. Journal of Geophysical Research: Space Physics, 120 (12), 10-926.

Fowler, C. M., McFadden, J., Hanley, K. G., Mitchell, D. L., Curry, S., and Jakosky, B. (2022). In-situ measurements of ion density in the Martian ionosphere: Underlying structure and variability observed by the MAVEN-STATIC instrument. Journal of Geophysical Research: Space Physics, 127 (8), e2022JA030352.

Fox, J. L., and Hać, A. B. (2009). Photochemical escape of oxygen from Mars: A comparison of the exobase approximation to a Monte Carlo method. Icarus, 204 (2), 527-544.

Halekas, J. S., Brain, D. A., Luhmann, J. G., and et al. (2017). Flows, fields, and forces in the Mars-Solar wind interaction. Journal of Geophysical Research: Space Physics, 122 (11), 11-320.

Halekas, J. S., Ruhunusiri, S., Harada, Y., et al. (2017). Structure, dynamics, and seasonal variability of the Mars-solar wind interaction: MAVEN Solar Wind Ion Analyzer in-flight performance and science results. Journal of Geophysical Research: Space Physics, 122 (1), 547–578.

Hall, B. E. S., Lester, M., S´anchez-Cano, B., Nichols, J. D., et al. (2016). Annual variations in the Martian bow shock location as observed by the Mars Express mission. Journal of Geophysical Research: Space Physics, 121 (11), 11-474.

Harnett, E. M., and Winglee, R. M. (2006). Three-dimensional multifluid simulations of ionospheric loss at Mars from nominal solar wind conditions to magnetic cloud events. Journal of Geophysical Research: Space Physics, 111 (A9).

Hellinger, P., andTrávníček, P. M. (2013). Protons and alpha particles in the expanding solar wind: Hybrid simulations. Journal of Geophysical Research: Space Physics, 118 (9), 5421–5430.

Holmström, M. (2010). Hybrid modeling of plasmas. Numerical Mathematics and Advanced Applications 2009. Springer, Berlin, Heidelberg, 451–458.

Holmström, M. (2022). Estimating ion escape from unmagnetized planets. Annales Geophysicae. Copernicus GmbH , 40 (1), 83-89.

Holmström, M., and Wang, X. D. (2015). Mars as a comet: Solar wind interaction on a large scale. Planetary and Space Science, 119 , 43-47.

Horaites, K., Andersson, L., Schwartz, S. J., Xu, S., Mitchell, D. L., Mazelle, C., et al. (2021). Observations of energized electrons in the Martian magnetosheath. Journal of Geophysical Research: Space Physics, 126 (4), e2020JA028984.

Inui, S., Seki, K., Sakai, S., Brain, D. A., Hara, T., McFadden, J. P., et al. (2019). Statistical study of heavy ion outflows from Mars observed in the martian-induced magnetotail by MAVEN. Journal of Geophysical Research: Space Physics, 124 (7), 5482-5497.

Jakosky, B. M., Brain, D., Chaffin, M., Curry, S., Deighan, J., Grebowsky, J., et al. (2018). Loss of the Martian atmosphere to space: Present-day loss rates determined from MAVEN observations and integrated loss through time. Icarus, 315 , 146-157.

Jakosky, B. M., Slipski, M., Benna, M., Mahaffy, P., Elrod, M., Yelle, R., et al. (2017). Mars' atmospheric history derived from upper-atmosphere measurements of 38Ar/36Ar. Science, 355 (6332), 1408-1410.

Kallio, E., Fedorov, A., Budnik, E., Barabash, S., Jarvinen, R., and Janhunen, P. (2008). On the properties of O^+ and O_2^+ ions in a hybrid model and in Mars Express IMA/ASPERA-3 data: A case study. Planetary and Space Science, 56 (9), 1204-1213.

Kar, J., Mahajan, K. K., and Kohli, R. (1996). On the outflow of O_2^+ ions at Mars. Journal of Geophysical Research: Planets, 101 (E5), 12747–12752.

Leblanc, F., Martinez, A., Chaufray, J. Y., Modolo, R., Hara, T., Luhmann, J., et al. (2018). On Mars's atmospheric sputtering after MAVEN's first Martian year of measurements. Geophysical Research Letters, 45 (10), 685-4691.

Ledvina, S. A., Brecht, S. H., Brain, D. A., and Jakosky, B. M. (2017). Ion escape rates from Mars: Results from hybrid simulations compared to MAVEN observations. Journal of Geophysical Research: Space Physics, 122 (8), 8391-8408.

Leelavathi, V., Rao, N. V., and Rao, S. V. B. (2023). Gravity wave driven variability in the Mars ionosphere-thermosphere system. Icarus, 115430 .

Lillis, R. J., Deighan, J., Fox, J. L., Bougher, S. W., Lee, Y., Combi, M. R., et al. (2017). Photochemical escape of oxygen from Mars: First results from MAVEN in situ data. Journal of Geophysical Research: Space Physics, 122 (3), 3815-3836.

Lundin, R., Barabash, S., Futaana, Y., Holmström, M., Perez-de-Tejada, H., and Sauvaud, J. A. (2013). A large-scale flow vortex in the Venus plasma tail and its fluid dynamic interpretation. Geophysical research letters, 40 (7), 1273–1278.

Lundin, R., Barabash, S., Futaana, Y., Sauvaud, J.-A., Fedorov, A., and de Tejada, H. P. (2011). Ion flow and momentum transfer in the Venus plasma environment. Icarus, 215 (2), 751–758.

395 Lundin, R., Zakharov, A., Pellinen, R., Borg, H., Hultqvist, B., Pissarenko, N., et al. (1989). First measurements of the ionospheric plasma escape from Mars. Nature, 341 (6243), 609-612.

Ma, Y. J., Dong, C. F., Toth, G., van der Holst, B., Nagy, A. F., Russell, C. T., et al. (2019). Importance of ambipolar electric field in driving ion loss from Mars: Results from a multifluid MHD model with the electron pressure equation included. Journal of Geophysical Research: Space Physics, 124 (11), 9040–9057.

400 Ma, Y. J., Fang, X., Nagy, A. F., Russell, C. T., and Toth, G. (2014). Martian ionospheric responses to dynamic pressure enhancements in the solar wind. Journal of Geophysical Research: Space Physics, 119 (2), 1272-1286.

Ma, Y. J., and Nagy, A. F. (2007). Ion escape fluxes from Mars. Geophysical Research Letters, 34 (8).

Marsch, K. H., E.and Mühlhäuser, Rosenbauer, H., Schwenn, R., and Neubauer, F. M. (1982). Solar wind helium ions: Observations of the Helios solar probes between 0.3 and 1 au. Journal of Geophysical Research: Space Physics, 87 (A1), 35–51.

405 Mazelle, C., Winterhalter, D., Sauer, K., Trotignon, J. G., Acuna, M. H., Baumgärtel, K., et al. (2004). Bow shock and upstream phenomena at Mars. Space Science Reviews, 111 (1), 115-181.

Modolo, R., Hess, S., Mancini, M., Leblanc, F., Chaufray, J. Y., Brain, D., et al. (2016). Mars-solar wind interaction: LatHyS, an improved parallel 3-d multispecies hybrid model. Journal of Geophysical Research: Space Physics, 121 (7), 6378-6399.

Nilsson, H., Zhang, Q., Wieser, G. S., Holmström, M., Barabash, S., Futaana, Y., et al. (2021). Solar cycle variation of ion escape from Mars. 410 Icarus, 114610.

Ramstad, R., and Barabash, S. (2021). Do intrinsic magnetic fields protect planetary atmospheres from stellar winds? lessons from ion measurements at Mars, Venus, and Earth. Space Science Reviews, 217 (2), 1-39.

Ramstad, R., Barabash, S., Futaana, Y., Nilsson, H., and Holmström, M. (2016). Effects of the crustal magnetic fields on the Martian atmospheric ion escape rate. Geophysical Research Letters, 43 (20), 10-574.

415 Regoli, L. H., C. Dong, Y. M., Dubinin, E., Manchester, W. B., Bougher, S. W., and Welling, D. T. (2018). Multispecies and Multifluid MHD approaches for the study of ionospheric escape at Mars. Journal of Geophysical Research: Space Physics, 123 (9), 7370-738.

Rojas-Castillo, D., Nilsson, H., and Stenberg Wieser, G. (2018). Mass composition of the escaping flux at Mars: MEX observations. Journal of Geophysical Research: Space Physics, 123 (10), 8806-8822.

Stansby, D., Perrone, D., Matteini, L., Horbury, C. S., T. S.and Salem. (2019). Alpha particle thermodynamics in the inner heliosphere fast 420 solar wind. Astronomy Astrophysics, 623 , L2.

Szegö, K., Glassmeier, K. H., Bingham, R., Bogdanov, A., Fischer, C., Haerendel, G. ., and Zank, G. (2000). Physics of mass loaded plasmas. Space Science Reviews, 94 (3), 429-671.

Vignes, D., Acu ˜na, M. H., Connerney, J. E. P., Crider, D. H., Reme, H., and Mazelle, C. (2002). Factors controlling the location of the bow shock at Mars. Geophysical research letters, 29 (9), 42-1.

425 Vignes, D., Mazelle, C., Rme, H., and et al. (2000). The solar wind interaction with Mars: Locations and shapes of the bow shock and the magnetic pile-up boundary from the observations of the MAG/ER experiment onboard Mars Global Surveyor. Geophysical Research Letters, 27 (1), 49-52.

Von Steiger, R., J. Geiss, G. G., and Galvin, A. B. (1995). Kinetic properties of heavy ions in the solar wind from SWICS/Ulysses. Space Science Reviews, 72 (1), 71–76.

430   Weber, T., Brain, D., Xu, S., Mitchell, D., Espley, J., Mazelle, C., et al. (2021). Martian crustal field influence on O^+ and O_2^+ escape as measured by MAVEN. Journal of Geophysical Research: Space Physics, 126 (8), e2021JA029234.

Wilson, I. L. B., Stevens, M. L., Kasper, J. C., Klein, K. G., Maruca, B. A., Bale, S. D., et al. (2018). The statistical properties of solar wind temperature parameters near 1 au. The Astrophysical Journal Supplement Series, 236 (2), 41.

Xu, S., Mitchell, D. L., Ma, Y., Weber, T., Brain, D. A., Halekas, J., et al. (2021). Global ambipolar potentials and electric fields at Mars

435   inferred from MAVEN observations. Journal of Geophysical Research: Space Physics,126 (12), e2021JA029764.

Xu, S., Schwartz, S. J., avid L. Mitchell, Horaites, K., Andersson, L., Halekas, J., et al. (2021). Cross-shock electrostatic potentials at Mars inferred from maven measurements. Journal of Geophysical Research: Space Physics,126 (3), e2020JA029064.648

Zhang, Q., Gu, H., Cui, J., Cheng, Y. M., He, Z. G., Zhong, J. H., et al. (2020). Atomic oxygen escape on Mars driven by electron impact excitation and ionization. The Astronomical Journal , 159 (2), 54.